PHYSICAL REVIEW B VOLUME 20, NUMBER 12 15 DECEMBER 1979

Quantitative analysis of low-energy-electron diffraction: Application to Pt(111)

D. L. Adams and H. B. Nielsen
Institute of Physics, University of Aarhus, DK-8000 Aarhus C, Denmark

M. A. Van Hove
Materials and Molecular Research Division, Lawrence Berkeley Laboratory, Berkeley, California 94720 and Department of Chemistry, University of California, Berkeley, California 94720

(Received 21 May 1979)

A method is described for quantitative analysis of low-energy-electron diffraction (LEED) intensity-energy spectra by comparison of experimental spectra with spectra calculated using a dynamic theory of LEED. The method involves a minimization of the variance of the fit between experimental and calculated spectra as a function of the calculational variables, both structural and nonstructural, leading to determination of optimum parameter values. Correlation between the variables is taken into account. The method is applied to extensive, new experimental LEED data for Pt(111). It is shown quantitatively that the variance of the fit depends strongly on the value of a single structural variable, $d_\perp$, the first interlayer spacing, but weakly on the values of three nonstructural variables, V_0, the inner potential, V_{im}, the absorption potential, and Θ_D, the Debye temperature. The analysis leads to an optimum value of $d_\perp = 2.29$ Å, corresponding to a 1% expansion of the first layer spacing, with an estimated error of ± 0.1 Å. This result is in good agreement with the earlier studies of Kesmodel and co-workers.

I. INTRODUCTION

The work described in this paper constitutes the first of a projected series of studies of platinum surfaces. It concerns the most simple case of the clean Pt(111) surface, for which previous low-energy-electron diffraction (LEED) studies have shown that the surface structure has the same two-dimensional periodicity as the bulk, and for which both LEED and ion-scattering studies have shown that the first interlayer spacing has the bulk value to within a few percent.[1-3]

Since the Pt(111) surface structure appeared to be quite well established, it seemed to us to be a useful starting point for testing our LEED experimental and computational procedures with a view to their later application to structurally more complex systems such as the reconstructed Pt(110) surface.[4] In the course of the work, however, we were led to investigate several questions of general importance concerning the quantitative analysis of LEED data. The results of these investigations form the basis for this paper.

The most widely used and accepted procedure for surface-structure determination via analysis of LEED measurements is a trial-and-error method, in which the measured intensities of (hk) diffracted beams, usually in the form of intensity-energy spectra, [(hk) beam intensity versus incident beam energy] are compared with intensities calculated for a trial surface structure having the appropriate two-dimensional periodicity, as determined from the LEED pattern. An accurate calculation of diffracted beam intensities requires in principle a self-consistent construction of the electron wave field in the solid, taking into account all multiple scattering processes, from which the intensities of the diffracted beams in the vacuum can be obtained. The calculation necessarily involves simplifying assumptions concerning the interaction of the incident electron with the surface region of the solid and involves several parameters characterizing that interaction, whose values can only be fixed via comparison with experiment. Thus the procedure of comparison involves variation over the value of these nonstructural parameters, in addition to variation over the values of the structural parameters.

In the last few years, the development by Pendry,[5] Van Hove and Tong,[6] among others, of relatively fast computational schemes for calculation of LEED intensities, following the accurate, but demanding, calculations of Jepsen, Marcus, and Jona[7] have created the ability to range more widely over the values of the calculational parameters than was previously practical in terms of computational expense. It is still the case, however, that the computational requirements are too large to permit automatic variation of parameter values to find a best fit between experimental and calculated intensities, as is carried out, for example, in least-squares structural refinement in x-ray diffraction analysis. Accordingly, parameter variation is expensive in computational time, requiring repetitive calculations, and the risk exists that the search procedure may fail to range sufficiently widely to find the optimum parameter values.

It is evident that a considerable simplification of the parameter search could be achieved if the number of parameters could be effectively reduced. In fact, it has been generally assumed in analyses of LEED data via model calculations that the fit between experimental and calculated intensities depends more strongly upon the values of the *structural* parameters than upon the nonstructural parameters, which are typically fixed at presumed reasonable values, except for a fitting of the muffin-tin constant. Some support for this practice has been provided by comparisons to experiment involving variation of the nonstructural parameters, but a quantitative assessment of the relative importance of structural and nonstructural parameters has been lacking because of the imprecise nature of the comparison procedures typically used in LEED studies. A major conclusion of the present study is that the relative importance of the structural parameters in determining the fit to experiment is established via quantitative comparison procedures.

Until quite recently, there has been an apparent reluctance to apply to LEED analyses the kind of quantitative, reliability index assessment of the comparison between experiment and calculations that is standard practice in x-ray crystallography. This reluctance can probably be attributed in part to the inevitable lack of truly quantitative agreement resulting from the approximations made in the calculations and the difficulties in obtaining precise measurements. There is a prevalent opinion that in the absence of quantitative agreement a visual comparison of spectral peak positions and line shapes is more reliable than a representation of the fit by a single number. In the case of a small data base, such a visual assessment of the comparison is feasible, but possibly ambiguous. Clearly the risk of finding an apparently acceptable but incorrect structure is minimized if the comparison involves a large data base, but a visual assessment of the effects of variations of several parameters is then less practical, and more objective assessment is needed.

Objective measures of the agreement between experimental and calculated LEED intensities have been proposed by Ignatiev *et al.*[8] and investigated by Van Hove, Tong and Elconin,[9] Zanazzi and Jona,[10] and in a different context by Adams and Landman.[11] The somewhat complicated reliability index (r factor) proposed by Zanazzi and Jona,[10] designed to emphasize spectral peak positions and line shapes and involving both first and second derivatives with energy of intensity-energy spectra, has been further applied recently by Mitchell and coworkers.[12-14] In most cases, the dependence of the r factors on the parameter values of the calculations was found to be quite well behaved, and reasonable optimum parameter values were determined from the minima of r factor plots.

In the present work, we demonstrate that r factors defined in terms of the *variance* of the fit between experimental and calculated LEED intensities, and related to the simple r factors used in x-ray crystallography, are quite adequate for the determination of both structural and nonstructural parameters. In addition we discuss the assessment of the accuracy of the parameter value determination, including the effects of correlation between the parameters. Specifically, we use r factor assessment of the fit between experimental and calculated intensity-energy spectra to examine the influence of the platinum potential used in the calculations, and the accuracy of its representation; the effect on the fit of the inner potential V_0, absorptive potential V_{im}, Debye temperature Θ_D, and a single structural parameter, the first interlayer spacing $d_\perp$, and to determine optimum values for $d_\perp$, V_0, V_{im}, and Θ_D.

The organization of the remainder of this paper is as follows. Experimental procedures used in measurement of intensity-energy spectra for Pt(111) are described in Sec. II. In Secs. III and IV, the basic assumptions of the theory and some details of the computational schemes are briefly summarized. Quantitative procedures for comparison of experiment and theory are described in Sec. V and applied to the analysis of the experimental intensity-energy spectra for Pt(111). A discussion of this work and some conclusions are presented in Sec. VI. Plots of experimental and calculated intensity-energy spectra corresponding to near-optimum parameter values are shown in the Appendix, with the purpose of enabling the reader to relate the determined r factor values to a visual judgment of the extent of agreement between experiment and theory.

II. EXPERIMENTAL PROCEDURES

The experimental apparatus used in the present study is an ion-pumped, metal, ultrahigh-vacuum system, base pressure $\approx 5\times10^{-11}$ Torr, constructed to our design by Vacuum Generators Ltd., and including four-grid LEED optics and electron gun manufactured by Varian Associates Inc. The main experimental chamber is constructed of mumetal; the magnetic field in the region between the sample and the LEED optics measured $\approx$ 20 mG.

The Pt(111) sample was mounted on a Vacuum Generators manipulator, which has facilities for sample rotation about the main, vertical axis of the chamber and also about a horizontal axis coincident with the axis of the LEED optics. The manipulator permits translation of the sample along

the vertical axis and along two orthogonal horizontal axes, and also permits tilting of the sample in any direction about a pivot point near the top of the manipulator. By means of these facilities, it is possible to control the relative geometry of the incident electron beam and the sample surface to better than 0.1° in terms of the angles of incidence and azimuth. The tilt adjustment was found to be useful in correcting for small misalignments of the sample on its supports to that the angle of incidence could be defined purely in terms of a rotation about the main vertical axis.

The Pt(111) sample was kindly supplied to us by Mr. Bernard Addis of Cornell University in the form of a ribbon of dimensions $\approx 0.25 \times 5 \times 15$ mm^3, oriented and polished. The sample was spot-welded to molybdenum supports and attached to a sample support assembly of our construction, which includes facility for electron bombardment heating of the reverse side of the sample. The manipulator also included provision for liquid nitrogen cooling of the sample. With out support assembly, temperatures of ≈ 85°K can be achieved. The temperature of the sample was measured, using a tungsten-rhenium thermocouple spot-welded at the middle of a sample edge.

After installation of the Pt(111) sample in the vacuum system, Auger electron spectroscopy (AES) measurements, using the LEED optics and an ancillary electron gun at $\approx 15°$ incidence, indicated the main impurities to be C, P, Ca, and S. The carbon was removed by heating for several hours at 1100°C in 1×10^{-7} Torr of oxygen. The most persistent impurity was sulfur, which was only removed by extended heating to 1250°C in vacuum for several days. During the LEED measurements, the sample was flashed to 1250°C to remove adsorbed impurities before each measurement of an intensity-energy spectrum. AES measurements made shortly after taking the LEED spectra indicated that the impurity level was less than 1% of a monolayer of detectable impurities.

Intensity-energy spectra for individual (hk) diffracted beams were obtained via measurement of the light intensity from the fluorescent screen of the LEED optics, using a Photo Research spot photometer of 0.5° angular acceptance. In the case of the nonspecular (hk) beams, the beam movement with changing incident electron energy was manually tracked by sighting through the spot photometer viewfinder. Accurate measurements could be made in this way using sufficiently slow scan rates of the incident beam energy of less than 1 eV sec^{-1}. Repeated measurements were made for each (hk) beam to confirm the reproducibility of the spectra. The measured spectra were converted to digital form and normalized for the measured variation of the incident electron beam current with changing energy. The spectra were all measured at room temperature.

In order to avoid errors in the measured spectra due to inaccuracies in settings of the angles of incidence θ and azimuth ϕ, particular care was taken to ensure that the set of intensity spectra for given θ, ϕ showed the appropriate symmetry relationships. Since the computational schemes used for calculating intensity-energy spectra rely for their efficiency on exploitation of special symmetry conditions, care was also taken in setting the appropriate angular values.

As discussed by Holland and Woodruff,[15] for arbitrary θ, ϕ, the diffracted intensities do not reflect the symmetry of the surface structure. However, the reciprocity theorem is applicable, implying that $I_{00}(E, \theta) = I_{00}(E, -\theta)$. This relationship was used to establish the true zero of incidence by comparison of specular-beam intensity-energy spectra for $\pm\theta$ values. In the case of Pt(111), as illustrated in the sketch of Fig. 1, the surface structure has a threefold rotational symmetry axis in the surface normal direction and a set of

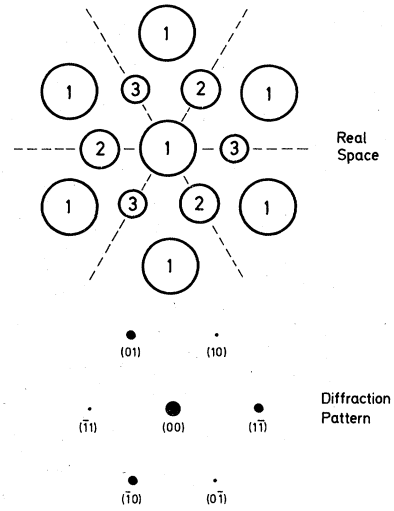

FIG. 1. Sketches of the Pt(111) surface structure and (below) the corresponding diffraction pattern. In the top sketch, circles numbered 1, 2, and 3 illustrate the relative positions of atoms in the first, second, and third layers. The orientation of the crystal was as is shown in the sketch, with a mirror plane (normal to the dashed line) coincident with the horizontal plane of the vacuum system and coincident with the plane of incidence of the incident electron beam. This orientation we define as $\phi = 0°$. The threefold rotational symmetry and mirror-plane symmetry present for $\phi = 0°$ *and* $\theta = 0°$ is shown schematically in the diffraction pattern. It is noted that exactly the same symmetry exists for $\phi = 180°$, but that distinction between $\phi = 0°$ and 180° can be made via comparison of experimental and calculated intensity spectra.

three equivalent mirror planes, which contain this axis. At normal incidence, the diffracted beam intensities exhibit the full symmetry of the surface spacegroup, allowing a further check to be made of the setting of zero incidence by comparison of intensity-energy spectra of symmetry equivalent (hk) beams. For nonnormal incidence, but at an azimuthal angle of $\phi = 0$ as defined in Fig. 1, the plane of incidence coincides with one of the mirror planes, and so this symmetry element is retained in the intensities. This condition was exploited to set the zero of azimuth.

By using the symmetry conditions and by comparing intensity spectra taken for small differences in angular settings, we believe that the angular values were determined to an absolute accuracy of $\pm 0.2°$. It is also noted that the successful application of symmetry conditions (symmetry equivalent beams *were* equivalent to within a few percent in relative intensities, and peak positions in the spectra were reproduced to better than 1 eV) implies that the response of the fluorescent screen was uniform across its area.

Intensity-energy spectra were measured for twelve (hk) beams (some of which were symmetry equivalent at normal incidence) at angles of incidence $\theta = 0$, $\pm 4°$, $\pm 10°$, and $\pm 16°$, and for azimuthal angle $\phi = 0$ in each case. These spectra are shown together with the corresponding calculated spectra in the Appendix. The energy ranges of the spectra were limited by the emergence threshold conditions for the particular (hk) beams and by the experimental arrangement. The fluorescent screen subtends a solid angle of 96° about the axis of the LEED optics, but a central region of the screen is partially obscured by our sample manipulator and support assembly. We note that due to the close-packed nature of the Pt(111) surface, threshold emergence energies are quite large; in general, intensities were not measured below 60 eV. In comparing calculated and experimental spectra, the maximum energy range considered is 60–280 eV.

Finally, we note that the present intensity spectra compare reasonably well with the data of Stair *et al.*[1] obtained using a photographic technique, although the present data set is more extensive. Over the common range of the data sets spectral peak positions are consistent to within a few eV.

III. CALCULATIONAL-MODEL ASSUMPTIONS AND PARAMETERS

Calculations of (hk) beam intensities were based on the conventional model of LEED, involving solution of a one-electron Schrödinger equation for a model system, in which the ion-core scattering potential has the muffin-tin form and in which the incident electron is attributed a complex self-energy inside the solid to simulate many-body interactions.

No effects specific to the surface were included in the electron-solid interaction potential. The surface potential barrier was treated as a nonreflecting (but refracting) potential step.

The ion-core scattering potential was obtained as a tabulation of $V(r)$ from the relativistic augmented-plane-wave (RAPW) calculation of Andersen,[16] in which Slater exchange was used. Partial-wave phase shifts were calculated from $V(r)$ by numerical integration of the Schrödinger equation in the usual manner. In some calculations, relativistic effects were approximated by use of "quasirelativistic" phase shifts, obtained by averaging spin-up and spin-down relativistic phase shifts calculated using the Andersen potential and kindly supplied to us by Roland Feder.[17]

The complex self-energy was represented in our calculations by a real part, the muffin-tin zero with respect to the vacuum level, V_0 ("inner potential") and an imaginary part, V_{im} ("absorption potential"). V_0 and V_{im} were treated as energy-independent parameters with values to be fixed by comparison of experimental and calculated intensity spectra. The absorption potential was taken to set in abruptly at a distance above the top layer of ion cores of one-half the bulk interlayer spacing.

The effect of thermal vibrations was treated in the usual approximation of renormalization of the ion-core scattering matrices by a Debye-Waller factor. Isotropic thermal vibrations were assumed, and no distinction was made between the vibrational properties of different layers. Thus a single Debye temperature was required, with value again to be fixed via comparison of experimental and calculated intensity spectra.

As discussed in Sec. IV the computed (hk) intensities are believed to be numerically accurate ($\approx 0.1\%$) within the above model assumptions at reasonably low energies. At higher energies, computational limitations to the number of partial-wave phase shifts that could be used in describing scattering from the ion-cores were a source of error. This problem is illustrated in Fig. 2, where the ion-core differential scattering cross section for normal incidence and diffracted angles of 0° and 180° is shown as a function of energy for different total numbers of phase shifts used in its calculation. As can be seen in Fig. 2, convergence in the cross section is achieved for calculations using 12 or more phase shifts at all energies up to 280 eV. In our calculations, how-

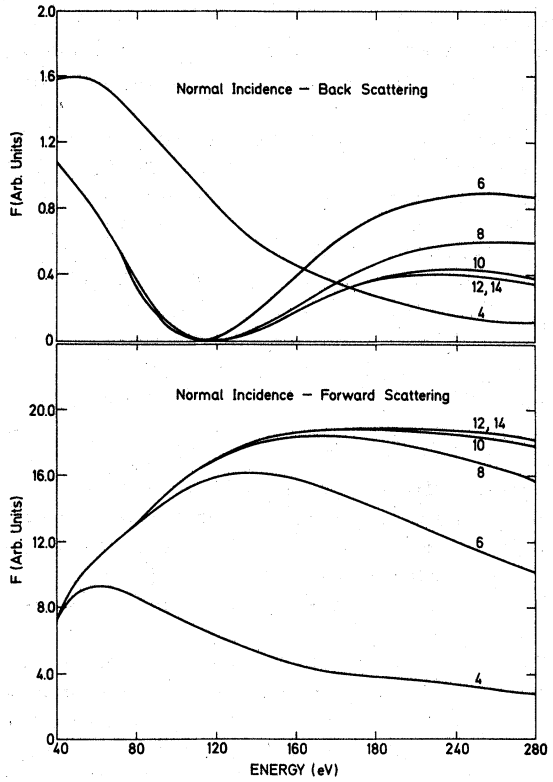

FIG. 2. Atomic scattering factor (differential scattering cross section) versus electron energy, calculated using the Andersen[16] Pt muffin-tin potential, for different total numbers of partial-wave phase shifts. Top panel for backward scattering, bottom panel for forward scattering. Normal incidence in each case.

ever, maximum numbers of 10 and 8 phase shifts, respectively, were used in calculations of normal and nonnormal incidence intensity spectra. The results of Fig. 2 suggest that the former spectra are likely to be in error at energies above 180 eV and the latter above 120 eV. While the magnitude of the error cannot be determined, its consequences for the fit to experimental spectra is evaluated in Sec. V.

IV. COMPUTATIONAL PROCEDURES

Diffracted-beam intensities were calculated using a version of Pendry's[5] *renormalized forward scattering* (RFS) algorithm.[6]

The RFS algorithm involves calculation of layer scattering matrices for each nonequivalent layer via a matrix inversion procedure, based essentially on the original formulation of Beeby,[18] which takes into account multiple scattering processes within the layer to infinite order. Within each layer, the electron wave field is expanded in a basis of spherical harmonics. The accuracy, with which the layer scattering matrices are obtained, is determined by the number of spherical harmonics used in the representation, and by cutoff criteria which determine convergence of lattice sums. The latter were chosen in our calculations to ensure convergence of the matrix elements to better than 0.1%.

The electron wave field in the region of constant potential between the layers is expanded in a plane-wave (beam) basis for reasons of computational efficiency, including exploitation of symmetry conditions. The layer scattering matrices are obtained in the plane-wave representation via a unitary transformation. The accuracy of the plane-wave expansion depends upon the number of beams used, which is determined for each incident electron energy. All propagating (hk) beams are included together with those evanescent beams whose amplitudes decay by less than a specified ratio in propagating from one layer to the next. This cutoff ratio was set conservatively in the calculations at 10^{-6}, ensuring convergence of the plane-wave expansion at all energies used. This led to inclusion of 61 beams at the highest energy of 280 eV. In the normal incidence calculations, the threefold rotational symmetry and mirror-plane symmetry enabled the 61 beams to be reduced to 15 symmetry nonequivalent beams, with consequent large reductions in computational time and storage. The mirror-plane symmetry for $\phi = 0$, $\theta \neq 0$ allowed the 61 beams to be reduced to 35.

In the RFS algorithm, the layer scattering matrices are used to obtain the diffracted beam intensities via a perturbation expansion of the total reflectivity in orders of backward scattering processes. The accuracy of this part of the calculation is determined by convergence criteria, which determine, firstly, for each order of the perturbation expansion how deeply into the solid the electron propagation is followed, depending upon damping of the wavefield by elastic and inelastic scattering, and secondly, the number of orders of the perturbation expansion. The convergence criteria were again set conservatively in the calculations, with the result that the diffracted beam intensities were converged to better than 0.1% at all energies.

As a check on the numerical reliability, intensity spectra for normal incidence were also calculated, using Van Hove and Tong's modification of Pendry's *layer-doubling* algorithm. In this procedure, layer scattering matrices are first calculated in a similar manner to that used in the RFS scheme. Multiple scattering processes between the layers, however, are summed over

in a different manner. In the layer-doubling algorithm, a total scattering matrix is first obtained via an iterative process for a slab of the bulk of the solid 2^ν layers thick, where ν is the number of iterations. The total scattering matrix for the surface layer plus bulk is obtained in a final layer-doubling step. In each layer-doubling step, multiple scattering processes between the layers are included to infinite order via a matrix-inversion procedure. The accuracy of this part of the calculation is limited only by the number of iterations used, if sufficient beams are included to ensure convergence of the plane-wave expansion between the layers. In our calculations, the diffracted beam intensities were converged to better than 0.1%, typically after four or five iterations, including the final addition of the surface layer.

To compare the results of the RFS and layer-doubling algorithms, normal incidence intensity spectra were calculated for all the emergent beams in the energy range 60–280 eV. Eight partial-wave phase shifts were used in each calculation; 61 beams were used, reduced by symmetry to 15 in the RFS calculation and to 35 in the layer-doubling calculation. The results of the two calculations agreed to within ±0.2% for all beams at all energies. While this agreement does not establish the absolute reliability of the calculations, because of the similarities in calculation of the layer scattering matrices, it clearly provides grounds for some confidence in their reliability.

For comparison with the experimental results, intensity spectra were calculated using the RFS scheme for the 12 measured (hk) beams in the energy range 60–280 eV for angles of incidence $\theta = 0°$, ±4°, ±10°, and ±16°, and for $\phi = 0$ in each case. For the normal incidence spectra, the computer storage reduction achieved by exploitation of symmetry enabled the use of ten phase shifts. Eight phase shifts were used in the calculations for non-normal incidence. Each computer run involved calculation of the intensity spectra for all emergent beams for given θ and ϕ. Since the calculation of the layer scattering matrices, comprising a large fraction of the total calculation, is independent of the layer spacings, intensity spectra for typically five values of the first-layer spacing were calculated in each run. In the case of nonnormal incidence, spectra for $\pm\theta$ were efficiently calculated in the same run, without recalculation of the layer scattering matrices, via calculations for $\pm\theta$, $\phi = 0°$ and $\pm\theta$, $\phi = 180°$ and interchanging h and k indices in the latter case. The experimental uncertainty in the setting of ϕ as 0° or 180° (see Fig. 1) was removed by comparison of experimental and calculated spectra.

Intensity-energy spectra were calculated as described above for a range of values of the nonstructural parameters $V_{\rm im}$ and Θ_D and for different numbers of partial-wave phase shifts. Choice of optimum parameter values including $d_\perp$ and V_0 was made by comparison with experimental spectra, as described in Sec. V.

Finally, we note that each computer run as described above for fixed values of $V_{\rm im}$ and Θ_D required ≈ 65 000 words of central processor unit (CPU) memory. The 61 beams, 10 phase shifts, normal incidence runs required ≈ 20 min and the nonnormal incidence, 61 beams, 8 phase shifts runs ≈ 50 min on the Aarhus CDC 6400 computer.

V. COMPARISON OF EXPERIMENT AND THEORY

In this section, we describe the procedure used to determine optimum parameter values and estimates of their accuracy via comparison of experimental and calculated intensity-energy spectra. We concentrate almost entirely on the analysis of the five (hk) experimental spectra for normal incidence since the calculated spectra are independent of V_0 for this case; the effect of varying V_0 is simply to translate the relative energy zeros of the calculated and experimental spectra. In fact, the spectra for nonnormal incidence were calculated after determining the optimum value of V_0 as described below. The subsequent comparison of experimental and calculated spectra for nonnormal incidence served to confirm the parameter determination based on analysis of the normal incidence spectra.

Plots of experimental spectra and spectra calculated for near-optimum parameter values are given in the Appendix.

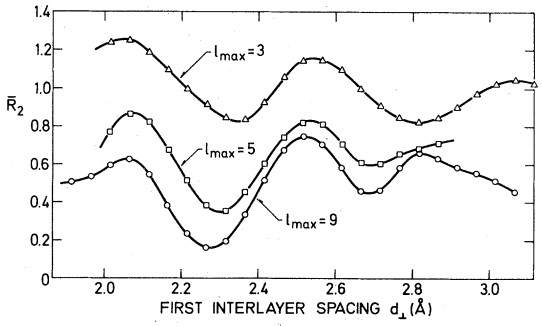

FIG. 3. Dependence of the fit between experimental and calculated intensity spectra for normal incidence on the value of the first-layer spacing, $d_\perp$, used in the calculations. The fit is characterized by $\bar{R}_2$ factor (see text). The different plots are for calculations using total number $(l+1)$ of phase shifts of 4, 6, and 10 respectively.

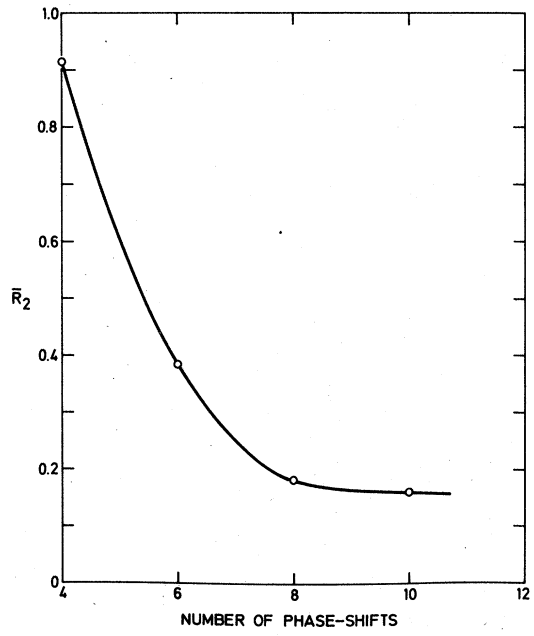

FIG. 4. Dependence of $\bar{R}_2$ on the total number of phase shifts used in the calculations. In each case the bulk value of 2.265 Å was used for the first-layer spacing $d_\perp$.

A. χ^2 and R factors

The agreement between individual experimental and calculated intensity spectra [i.e., for given (hk), θ, and ϕ] and the effect of parameter variation on the agreement was assessed in terms of the following statistics:

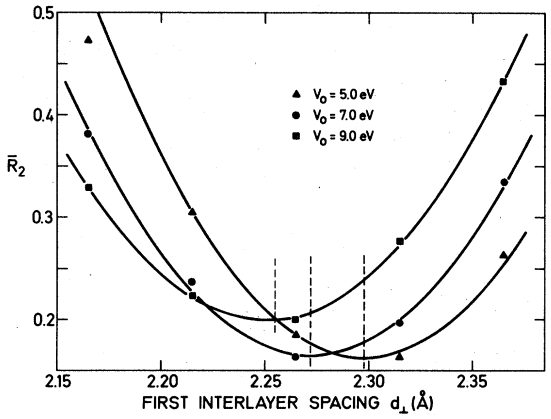

FIG. 5. Dependence of $\bar{R}_2$ on $d_\perp$ for different values of the inner potential V_0. Smooth curves in this and subsequent figures correspond to the least-squares parabolas fitted to the five data points closest to the minimum value of $\bar{R}_2$. Note the shift in the minimum value of $\bar{R}_2$ to lower values of $d_\perp$ for increasing values of V_0.

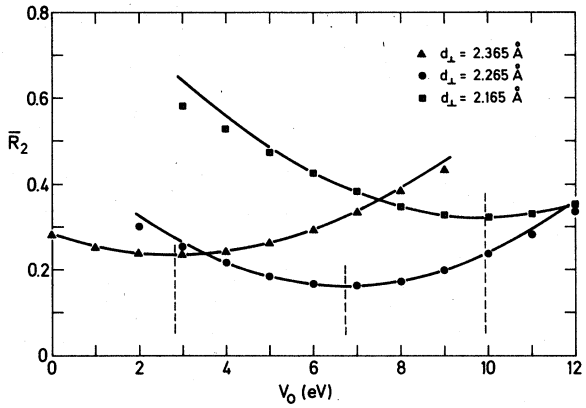

FIG. 6. Dependence of $\bar{R}_2$ on the inner potential V_0 for different values of $d_\perp$. Note the pronounced shift in the minimum of $\bar{R}_2$ to lower values of V_0 for increasing values of $d_\perp$.

$$\chi^2 = \int \{[wI_{\text{expt}}(E) - I_{\text{calc}}(E)]/\sigma(E)\}^2 \, dE \ , \qquad (5.1)$$

$$R_1 = \frac{\int [wI_{\text{expt}}(E) - I_{\text{calc}}(E)] \, dE}{\int [wI_{\text{expt}}(E)] \, dE} \ , \qquad (5.2)$$

$$R_2 = \frac{\int [wI_{\text{expt}}(E) - I_{\text{calc}}(E)]^2 \, dE}{\int (wI_{\text{expt}})^2 \, dE} \ . \qquad (5.3)$$

Optimum parameter values were obtained by minimizing χ^2 or R_2 with respect to the different parameters. Within the determined errors, these values were independent of which statistic was used. The reduced χ^2 factors R_1 and R_2 are used to provide a convenient basis for comparison with LEED studies of other systems. They correspond to the r factors used in x-ray crystallography.

In applications of Eq. (5.1), the unknown standard deviations $\sigma(E)$ of the data points were assumed

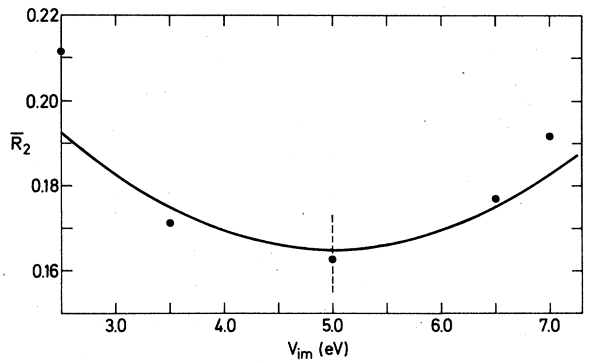

FIG. 7. Dependence of $\bar{R}_2$ on the absorptive potential V_{im} for fixed values of $d_\perp$ and V_0.

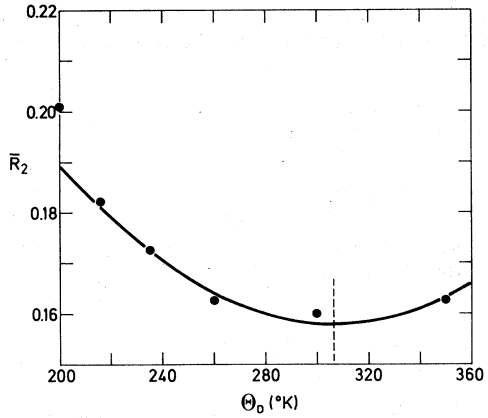

FIG. 8. Dependence of $\bar{R}_2$ on the Debye temperature Θ_D for fixed values of $d_\perp$, V_0 and $V_{\rm im}$.

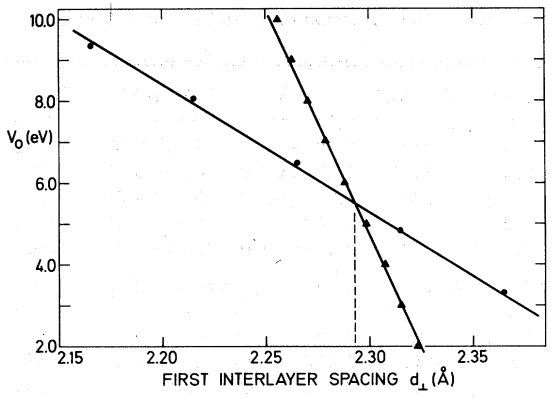

FIG. 10. Correlation of optimum values of $d_\perp$ and V_0. Circles: Plot of optimum V_0 $(d_\perp)$ vs $d_\perp$, corresponding to $\partial\chi^2/\partial V_0(d_\perp, V_0) = 0$. Triangles: Plot of optimum $d_\perp(V_0)$ vs V_0, corresponding to $\partial\chi^2/\partial d_\perp(d_\perp, V_0) = 0$. See text and Eq. (5.21).

equal, with rms value regarded as determined by the variance of the fit between experiment and theory, i.e.,

$$\sigma^2 = \left\langle\left(\int \sigma(E)^2\, dE \right)\right\rangle$$

$$\cong \left\langle\left(\int [wI_{\rm expt}(E) - I_{\rm calc}(E)]^2\, dE \right)\right\rangle . \qquad (5.4)$$

As noted previously, the absolute scale of the experimental intensities $I_{\rm expt}(E)$ is not known, and the scale of the calculated intensities $I_{\rm calc}(E)$ is liable to be in error, depending, for example, on the assumptions made concerning the onset of damping of the incident electron wave. Accordingly, Eqs. (5.1)–(5.4) include a scale factor, which we define as

$$w = \int I_{\rm calc}(E)\, dE \Big/ \int I_{\rm expt}(E)\, dE \ . \qquad (5.5)$$

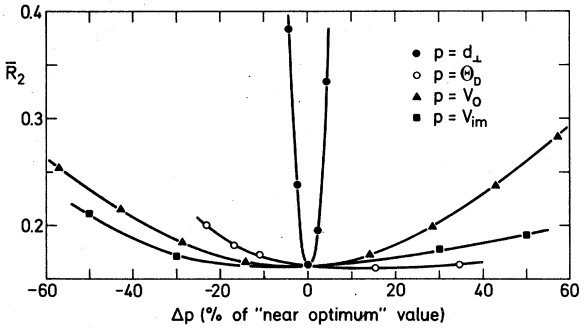

FIG. 9. Comparison of dependence of $\bar{R}_2$ on the calculational variables. The parameter values are expressed as percentages of their near-optimum values (see text).

Unless otherwise stated, numerical values of R_1 and R_2 in tables and figures to follow were obtained using Eq. (5.5) for each individual pair of experimental and calculated spectra. Values of w so obtained varied by almost a factor of three over the different spectra, due in part to the dependence of $\int I_{\rm calc}(E)\, dE$ on the parameters of the calculation, particularly $d_\perp$, and in part to experimental uncertainties in the relative scale factors of spectra for different beams and different angles of incidence.

To the best of our knowledge, spectrum by spectrum normalization of scale factors, as described above, has been used in all previous r factor analyses of LEED intensities. Although in the present case, the variation in scale factor did not appear to seriously affect the determination of optimum parameter values, it clearly leads to a risk of biasing the optimization procedure. Accordingly, in a more rigorous analysis based on minimization of χ^2, we have used a single, constant scale factor. It was found that an average

TABLE I. Optimum values of $d_\perp$ and V_0 from χ^2 analysis.

$d_\perp$ (Å)	V_0 (eV)
2.289 ± 0.009 [a]	5.42 ± 0.57 [a]
2.297 ± 0.008 [b]	5.30 ± 0.93 [b]
2.279 ± 0.008 [c]	5.73 ± 0.53 [c]
2.285 ± 0.010 [d]	5.83 ± 0.58 [d]

[a] Using $\langle\chi^2\rangle$ and constant scale factor $\bar{w}$.
[b] Using $\bar{R}_2$ and constant scale factor $\bar{w}$.
[c] Using $\langle\chi^2\rangle$ with individual beam scale factors w.
[d] Using $\bar{R}_2$ with individual beam scale factors w.

TABLE II. Optimization of $d_\perp$ and V_0 for different V_{im} and Θ_D.

V_{im} (eV)	Θ_D (°K)	$d_\perp$ (Å)	V_0 (eV)	$\bar{R}_{2\,min}$
2.5	260	2.292 ± 0.011	6.66 ± 0.51	0.2086
3.5	250	2.287 ± 0.010	6.50 ± 0.47	0.1706
5.0	260	2.285 ± 0.010	5.83 ± 0.58	0.1612
6.5	260	2.289 ± 0.011	5.89 ± 0.61	0.1760
7.5	260	2.287 ± 0.010	5.71 ± 0.70	0.1904
(Plot of $\bar{R}_{2\,min}$ vs V_{im} gives V_{im}(opt) = 5.18 ± 0.42 eV)				
5.0	200	2.285 ± 0.011	6.08 ± 0.56	0.2000
5.0	216	2.285 ± 0.010	6.13 ± 0.53	0.1819
5.0	230	2.285 ± 0.010	6.16 ± 0.52	0.1724
5.0	260	2.285 ± 0.010	5.83 ± 0.58	0.1612
5.0	300	2.286 ± 0.010	6.23 ± 0.50	0.1600
5.0	350	2.287 ± 0.010	6.24 ± 0.51	0.1624
(Plot of $\bar{R}_{2\,min}$ vs Θ_D gives Θ_D(opt) = 302 ± 16 °K)				

scale factor defined by

$$\bar{w} = \langle w_{hk} \rangle , \tag{5.6}$$

i.e., the average value of w of Eq. (5.5) over all the diffracted beams, was independent of the parameters of $I_{calc}(E)$ to within a few percent over a wide range of parameter values so that a single constant value of $\bar{w}$ could be used without biasing the optimization of the parameter values. We note that a similar beam average of a scale factor designed to minimize $\partial\chi^2/\partial w$, i.e.,

$$w = \frac{\int [I_{expt}(E) I_{calc}(E)]\, dE}{\int [I_{expt}(E)]^2\, dE} \tag{5.7}$$

was found to depend more strongly on the parameters of $I_{calc}(E)$, leading to our choice of the definitions of Eqs. (5.5) and (5.6).

Numerical calculations of χ^2, R_1, and R_2 as defined above were carried out by trapezoidal-rule integration on an energy grid of 2 eV, after interpolation of the spectra. The calculated spectra were initially on a grid of 0.3 Ry (4.08 eV), and the experimental spectra on a nonuniform grid of ≈1 eV.

In addition to χ^2, R_1, and R_2 values for individual pairs of spectra, average values were calculated for sets of difracted beams via the following definitions,

$$\langle \chi^2 \rangle (\bar{n}) = \frac{1}{b} \sum_{hk} \chi^2_{hk} , \tag{5.8}$$

where b is the number of (hk) beams in a set and $\bar{n}$ the average over the set of the number of data points n_{hk} per beam used in approximating the integrals of Eqs. (5.1)–(5.5), and

$$\bar{R}_{1,2} = \frac{1}{\bar{n} b} \sum_{hk} n_{hk} R_{hk} . \tag{5.9}$$

Equation (5.8) corresponds to an unweighted average over the beams of the set, whereas Eq. (5.9) corresponds to an average weighted by the energy ranges of comparison of the individual pairs of spectra. If the mean-square experimental intensities $\langle I^2_{hk}(E) \rangle$ of the different beams of the set were the same, and if a constant scale factor $\bar{w}$ were used, then $\langle \chi^2 \rangle$ and $\bar{R}_2$ would be related by

$$\bar{R}_2 = \langle \chi^2 \rangle / \bar{n} \bar{w}^2 \langle I^2_{hk}(E) \rangle . \tag{5.10}$$

B. Influence of structural and nonstructural parameters on the fit between experiment and theory

In this section, we demonstrate the relative importance of structural variables ($d_\perp$) and nonstructural variables (V_0, V_{im}, and Θ_D), and the influence of the accuracy of description of the scattering potential on the R factors defined in the previous section.

Inspection of $\bar{R}_1$ and $\bar{R}_2$ values calculated for a range of parameter values for the set of (hk) beams at normal incidence suggested that the optimum parameter values were close to $d_\perp = 2.265$ Å (bulk value), $V_0 = 7.0$ eV, $V_{im} = 5.0$ eV, and $\Theta_D = 260$°K. The calculated intensity spectra shown in the figures in the Appendix are in fact based on these "near-optimum" values. Refinement of these values, taking into account correlation between the variables, is described in following sections.

TABLE III. Optimization of $d_\perp$ and V_0 using χ^2 for individual beams at normal incidence.

Beam	Energy range (eV)	$d_\perp$ (Å)	V_0 (eV)
(10)	64–278	2.275 ± 0.006	5.76 ± 0.31
(1$\bar{1}$)	66–278	2.308 ± 0.012	4.59 ± 0.60
(2$\bar{1}$)	144–278	2.323 ± 0.009	5.84 ± 0.42
(20)	184–278	2.343 ± 0.011	5.91 ± 0.56
(2$\bar{2}$)	184–278	no well-defined minimum	
Unweighted mean values		2.313 ± 0.057	5.53 ± 0.56

TABLE IV. R_1 factors for individual beams. The numbers in parentheses give the energy ranges of comparison in eV.

θ \ hk	(00)	(10)	$(\bar{1}1)$	(01)	$(1\bar{1})$	(11)	$(\bar{1}2)$	$(2\bar{1})$	(20)	$(\bar{2}2)$	(02)	$(2\bar{2})$
0°		0.39 (214)	≡ (10)	≡ $(1\bar{1})$	0.38 (212)		≡ $(2\bar{1})$	0.22 (134)	0.24 (94)	≡ (20)	≡ $(2\bar{2})$	0.42 (94)
+4°	0.41 (218)	0.37 (48)	0.32 (206)	0.52 (202)	0.43 (204)	0.51 (104)	0.73 (62)	0.37 (134)				0.53 (126)
−4°	0.38 (218)	0.32 (206)	0.39 (120)		0.51 (198)	0.61 (110)	0.51 (150)	0.48 (58)		0.56 (128)		
+10°	0.37 (218)	0.40 (198)	0.41 (134)	0.40 (170)		0.50 (96)		0.27 (112)				0.51 (156)
−10°	0.34 (218)	0.28 (182)		0.25 (156)	0.46 (152)	0.72 (98)	0.41 (66)			0.39 (160)		
+16°	0.49 (218)	0.30 (210)			0.34 (120)			0.27 (46)	0.34 (120)			0.29 (78)
−16°	0.49 (214)	0.30 (100)	0.19 (132)	0.36 (218)			0.25 (78)			0.27 (30)	0.51 (120).	

The variation of $\bar{R}_2$ with $d_\perp$ for fixed, near-optimum values of the remaining variables is shown in Fig. 3. The figure includes plots based on calculations using a total of four, six, and ten phase shifts, respectively. As shown in the figure, each curve has a minimum in the vicinity of the bulk value of $d_\perp = 2.265$ Å. However, subsidiary minima are also present in the region 2.7–2.9 Å. These spurious minima presumably correspond to the "multiple coincidences" noted by Andersson and Pendry[19] in visual comparisons of experimental and calculated spectra.

We note that for the most accurate calculations, involving the use of ten phase shifts, the minimum near $d_\perp = 2.265$ Å is clearly dominant, but that discrimination between "real" and "spurious" minima becomes increasingly less certain as the accuracy of description of the scattering potential is decreased. A shift in the minimum to higher values of $d_\perp$ can also be seen in the plots.

The effect of the calculational accuracy with respect to the scattering potential is further demonstrated in Fig. 4, where $\bar{R}_2$ is plotted versus total number of phase shifts. The variation in $\bar{R}_2$ shown in the figure suggests that convergence in the $\bar{R}_2$ factor has been almost reached at ten phase shifts, and that the results at eight phase shifts are not far from convergence. These results can be seen to be consistent with the dependence of the accuracy of the scattering potential on the number of phase shifts, as shown in Fig. 2.

We note that calculations carried out using eight "quasirelativistic" phase shifts produced quite significant changes in spectral line shapes but only a small improvement in the overall agreement, yielding a value of $\bar{R}_2 = 0.175$, as compared to the value of $\bar{R}_2 = 0.180$ obtained using eight nonrelativistic phase shifts and $\bar{R}_2 = 0.163$ using ten nonrelativistic phase shifts.

The dependence of $\bar{R}_2$ on $d_\perp$, V_0, $V_{\rm im}$, and Θ_D is shown in Figs. 5–8, respectively. In Fig. 5, plots of $\bar{R}_2$ vs $d_\perp$ are given for several values of V_0, and in Fig. 6, plots of $\bar{R}_2$ vs V_0 are shown for several values of $d_\perp$. The correlation between these two variables is evident from Figs. 5 and 6.

The results of Figs. 5–8 are gathered together and replotted in Fig. 9. Each curve shows the variation of $\bar{R}_2$ with a single variable; the remaining variables being fixed at their near-optimum values. Comparison of the curves of Fig. 9 clearly shows that the fit between experiment and theory depends strongly upon the structural variable $d_\perp$ and relatively weakly on the nonstructural variables V_0, $V_{\rm im}$, and Θ_D.

C. Refinement of parameter values

In this section, we consider refinement of

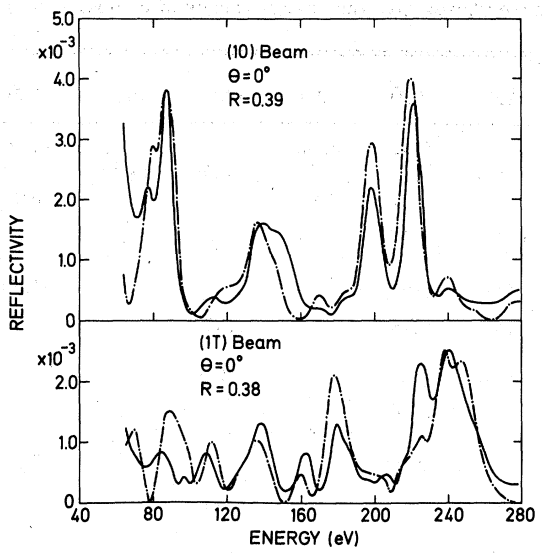

FIG. 11. Normal-incidence intensity spectra. The experimental spectra are shown as solid lines, the calculated spectra as dashed lines. The r factor is the R_1 factor.

parameter values based on tabulated values of χ^2 or R_2, taking into account correlation between the variables. In principle, the problem is to find the global minimum of χ^2 in a hyperspace of $n+1$

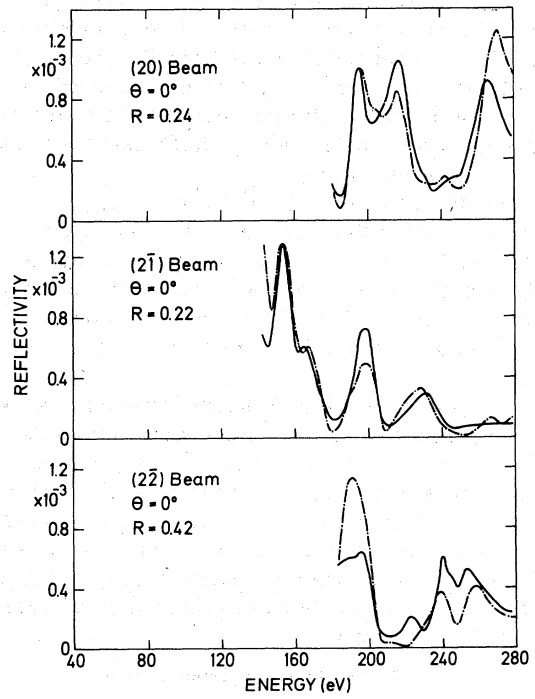

FIG. 12. Same as Fig. 11.

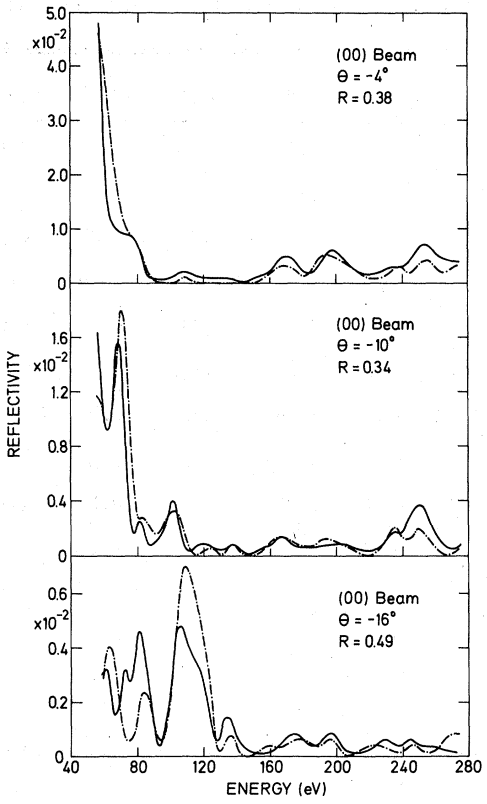

FIG. 13. Non-normal incidence spectra. The experimental spectra are shown as solid lines, the calculated spectra as dashed lines. The r factor is the R_1 factor.

dimensions for n variables. In practice, as demonstrated later, there is no significant dependence of the optimum values of $d_\perp$ and V_0 on the values of V_{im} and Θ_D. Thus the problem can be simplified to finding the minimum of χ^2 as a function of $d_\perp$ and V_0 for fixed values of V_{im} and Θ_D.

In recent papers, Mitchell and co-workers[12-14] have used contour plots of an r factor (proposed by Zanazzi and Jona[10]) vs $d_\perp$ and V_0 to locate the global minimum and hence best values of $d_\perp$ and V_0; the contour plots being constructed by interpolation between tabulated values.

The approach that we have taken is similar to that followed by the above authors, except that by use of χ^2 as defined in Eqs. (5.1) and (5.8), and by use of a constant scale factor $\bar{w}$ as defined by Eqs. (5.5) and (5.6), we consider that our approach is more correctly based on least-squares minimization. In particular, we are able to adopt the usual procedures for analysis of errors used in nonlinear minimization problems. In addition, we have designed an automatic search procedure using tabulated values of χ^2 which avoids explicit construction of contour plots.

Our procedure involves the basic assumption,

which is shown to be justified for the present data set, that in the vicinity of the minimum of the χ^2 plot, χ^2 can be expanded in a Taylor series in the parameters $d_\perp$ and V_0 in which second- and higher-order terms can be neglected. To simplify the notation, we make the substitutions:

$$z=\chi^2,\quad x=d_\perp,\quad y=V_0\ . \tag{5.11}$$

Then the Taylor series is to first order:

$$z(x+u,\ y+v)=z(x,y)+u\,\frac{\partial z}{\partial x}(x,y)+v\,\frac{\partial z}{\partial y}(x,y). \tag{5.12}$$

Following the method of least squares, the optimum values for the increments are $u=x_0-x$ and $v=y_0-y$, for which the function z is at a minimum, with coordinates z_0, x_0, y_0. Differentiation of Eq. (5.12) with respect to x and y then leads to the least-squares normal equations, which can be written in matrix form as

$$\begin{pmatrix}\partial z/\partial x\\ \partial z/\partial y\end{pmatrix}=\begin{pmatrix}\partial^2 z/\partial x^2 & \partial^2 z/\partial x\partial y\\ \partial^2 z/\partial x\partial y & \partial^2 z/\partial y^2\end{pmatrix}\begin{pmatrix}x-x_0\\ y-y_0\end{pmatrix},$$

or compactly as

$$\vec{g}=\underline{G}\vec{a}\ . \tag{5.13}$$

Inversion of Eq. (5.13) allows the minimum to be determined via

$$\vec{a}=\underline{G}^{-1}\vec{g}=\underline{\epsilon}\,\vec{g} \tag{5.14}$$

where the error matrix $\underline{\epsilon}=\underline{G}^{-1}$.

Within the above assumptions concerning truncation of the Taylor series, implicity involving a linearization of $I_{\rm calc}(E)$ as a function of $d_\perp$ and V_0, the standard deviations of x_0 and y_0 can be shown[20] to be given by

$$\sigma^2_{x_0}\cong\epsilon_{11}z_0/\bar{n},\quad \sigma^2_{y_0}\cong\epsilon_{22}z_0/\bar{n}\ , \tag{5.15}$$

where $\bar{n}$ is the number of data points used in forming χ^2, with each data point equally weighted.

A convenient procedure for determination of x_0, y_0, $\sigma^2_{x_0}$ and $\sigma^2_{y_0}$, which avoids numerical calculation of first and second derivatives of χ^2, is to take advantage of the equivalence[20] between the first-order Taylor expansion and a parabolic representation of χ^2 in terms of $d_\perp$ and V_0.

In the absence of correlation between $d_\perp$ and V_0, i.e., $\partial^2 z/\partial x\partial y=0$, the χ^2 plot in the above approximation is an elliptic paraboloid with elliptic axes along $d_\perp$ and V_0, i.e.,

$$c(z-z_0)=(x-x_0)^2/a^2+(y-y_0)^2/b^2\ . \tag{5.16}$$

In the event of a linear correlation between $d_\perp$ and V_0, i.e., $\partial^2 z/\partial x\partial y=\text{cons}$, which we justify below, then the paraboloid is rotated by an angle α about the x axis and is described by

$$z=z_0+a_1(x-x_0)^2+a_2(y-y_0)^2+2a_3(x-x_0)(y-y_0)\ , \tag{5.17}$$

where

$$a_1=\frac{1}{c}\left(\frac{\cos^2\alpha}{a^2}+\frac{\sin^2\alpha}{b^2}\right),$$

$$a_2=\frac{1}{c}\left(\frac{\cos^2\alpha}{b^2}+\frac{\sin^2\alpha}{a^2}\right),$$

$$a_3=\frac{1}{c}\left(\frac{1}{a^2}-\frac{1}{b^2}\right)\sin\alpha\cos\alpha\ . \tag{5,18}$$

Differentiation of Eq. (5.17) with respect to x and y, and use of Eqs. (5.13)–(5.15), leads to

$$\sigma^2_{x_0}=z_0\epsilon_{11}/\bar{n}=z_0a_1/[\,2(a_1a_2-a_3^2)]\bar{n} \tag{5.19}$$

and

$$\sigma^2_{y_0}=z_0\epsilon_{22}/\bar{n}=z_0a_2/[\,2(a_1a_2-a_3^2)]\bar{n}\ . \tag{5.20}$$

Thus by fitting tabulated values of $z(x,y)$, i.e., $\chi^2(d_\perp,V_0)$, to Eq. (5.17), z_0, x_0, y_0, $\sigma^2_{x_0}$, and $\sigma^2_{y_0}$ can be determined.

In practice, starting from a matrix of tabulated $z(x,y)$ values, we have found that the safest procedure to ensure the validity of the parabolic expansion of χ^2 is to fit a parabola according to Eq. (5.17) to each row and column of the matrix, i.e., z vs x for constant y or vice versa. If a given row or column does not contain a *tabulated* minimum, then the calculation is bypassed. Otherwise, vectors of $z_0(y)$ and $z_0(x)$ are assembled from the minima of the parabolas.

Setting the first derivatives of z from Eq. (5.17) equal to zero yields

$$x_0(y)-x_0=-a_3(y-y_0)/a_1$$

and

$$y_0(x)-y_0=-a_3(x-x_0)/a_2\ . \tag{5.21}$$

Substitution in Eq. (5.17) yields

$$z\big|_{\partial z/\partial y=0}=z_0(y)=z_0+(y-y_0)^2/2\epsilon_{22}$$

and

$$z\big|_{\partial z/\partial y=0}=z_0(x)=z_0+(x-x_0)^2/2\epsilon_{11}\ .$$

If the vectors of $z_0(y)$ and $z_0(x)$ contain minima as functions of y and x, respectively, then they are fitted to Eq. (5.22) to finally determine x_0, y_0, $\sigma^2_{x_0}$, and $\sigma^2_{y_0}$.

Finally, we note that an alternative procedure to find x_0, y_0 is to plot y vs $x_0(y)$, and $y_0(x)$ vs x. According to Eq. (5.21), this should yield two

straight lines, which intersect at y_0, x_0. Such a plot is given in Fig. 10 and demonstrates the validity of the assumed linear correlation of $d_\perp$ and V_0 in the region of the global minimum of the χ^2 plot.

The results of applying the above analysis to $\langle\chi^2\rangle(d_\perp, V_0)$ values calculated for the comparison with the five (hk) experimental intensity spectra at normal incidence are shown in Table I. Also included in the table are optimum parameter values derived using $\overline{R}_2$ in place of $\langle\chi^2\rangle$, and values derived using $\langle\chi^2\rangle$ and $\overline{R}_2$, in which the scale factor w was not constant but evaluated for each spectral comparison via Eq. (5.5). As can be seen from the table, the results in the last three rows do not in fact differ significantly from those in the first row, for which $\langle\chi^2\rangle$ with constant $\overline{w}$ was used, although only the latter is strictly justifiable.

D. Influence of V_{im} and Θ_D

In Sec. V C, the determination of optimum values of $d_\perp$ and V_0 assumed them to be uncorrelated with the values of V_{im} and Θ_D. This assumption was verified by repeating the analysis for different values of V_{im} and Θ_D, with results shown in Table II.

Since the intensity calculations for values of V_{im} and Θ_D other than 5.0 eV and 260°K, respectively, had not been saved at this stage of the work, the analysis was carried out using previously calculated values of $\overline{R}_2$ for the normal incidence spectra, in which individual scale factors w had been used.

By fitting the minimum $\overline{R}_2$ values (corresponding to optimum values of $d_\perp$ and V_0 in each case) as functions of V_{im} and Θ_D, optimum values of these variables were found to be

$$\Theta_D = 302 \pm 16°\text{K}, \quad V_{im} = 5.18 \pm 0.42 \text{ eV}.$$

E. Inclusion of spectra for non-normal incidence

The analysis described in Sec. V C was repeated using $\langle\chi^2(d_\perp, V_0)\rangle$ values averaged over the complete data set including both normal and non-normal incidence spectra. A constant weighting factor was used in forming $\langle\chi^2\rangle$.

We note that the procedure for taking into account the correlation between V_0 and $d_\perp$ is not strictly applicable in the case of the non-normal incidence spectra since the calculated intensities depend on V_0 due to the refraction of the incident electron beam on entering the solid. The results of the analysis, nevertheless, were in good agreement with the previous results for normal inci-

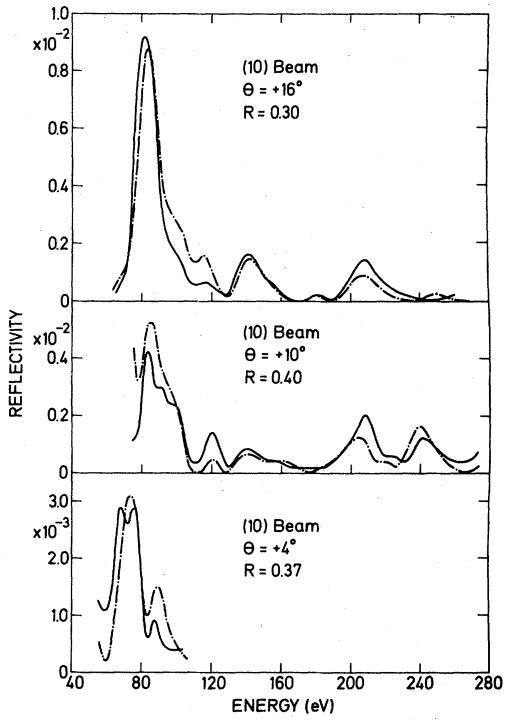

FIG. 14. Same as Fig. 13.

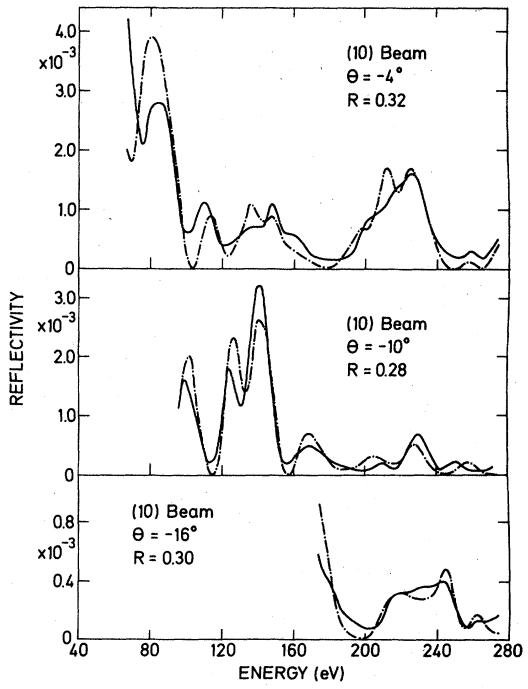

FIG. 15. Same as Fig. 13.

dence spectra. The optimum values of $d_\perp$ and V_0 were found to be

$$d_\perp = 2286 \pm 0.012 \text{ Å}, \quad V_0 = 7.01 \pm 0.53 \text{ eV}.$$

F. Average versus individual r factors

The analyses described in Secs. V B–V E involved the use of $\langle \chi^2 \rangle$ and $\overline{R}_2$ factors averaged over several (hk) beams. We have also investigated the use of individual diffracted beams in carrying out parameter determination.

The procedure described in Sec. V C was applied individually to the five (hk) beams for normal incidence, with results given in Table III.

There are two disturbing features of the results shown in the table. Firstly, the calculated standard deviations of $d_\perp$ are smaller than the deviation of the unweighted mean value given in the final row of the table. Secondly, no well-defined minimum was found for the $(2\bar{2})$ beam for physically acceptable values of V_0. We presume that the cause of these problems is the occurence of systematic errors, in part associated with determination of the optimum value of V_0.

In the case of the $(2\bar{2})$ beam, a local minimum of χ^2 was found in the tabulated χ^2 values in the region of $V_0 = 6.0$ eV, $d_\perp = 2.265$–2.315 Å but the global minimum was found at a negative value of V_0 with $d_\perp \cong 2.365$ Å. This appears to be a consequence of the small energy range of comparison for this beam and the existence of adjacent peaks in the experimental spectrum (see Fig. 12), which leads to multiple possibilities of matching with calculated spectra via a translation along the energy axis.

We believe that similar, but less drastic, effects may be responsible for the spread in optimum parameter values for the remaining beams of the set and note that Mitchell and co-workers[12–14] have also observed pathological behavior in r factor plots for individual beams, associated with variation in V_0.

It seems likely to us that in the case of r factors averaged over several beams, as used in previous sections, the possibility of systematic er-

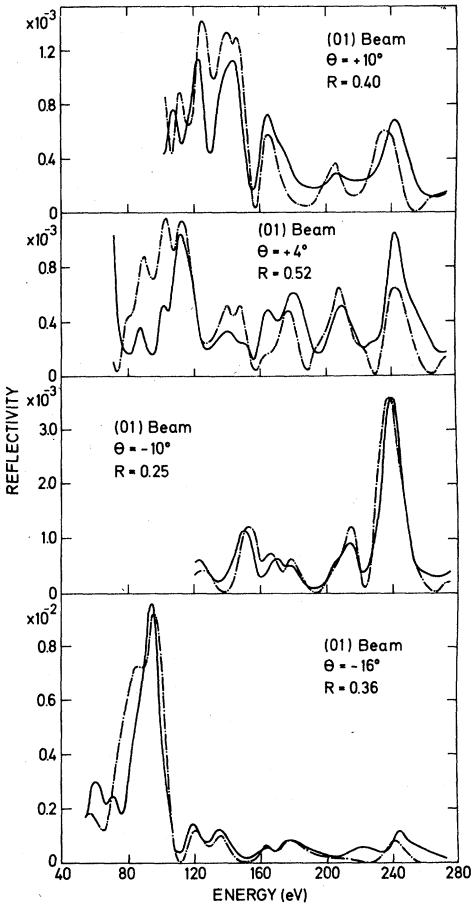

FIG. 16. Same as Fig. 13.

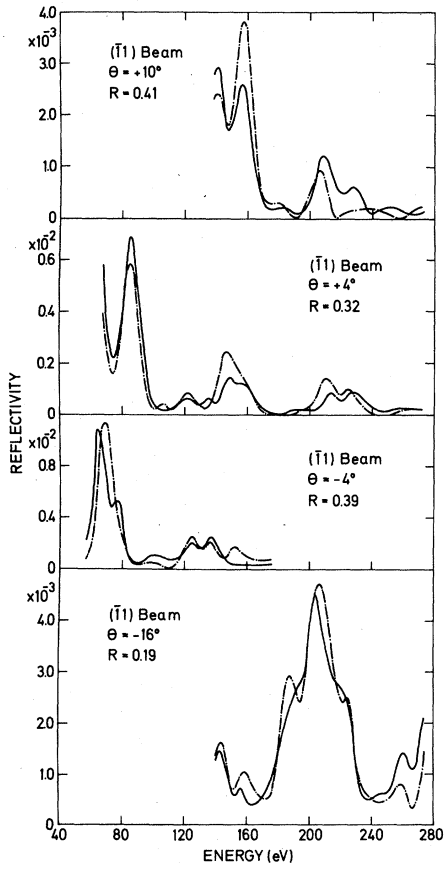

FIG. 17. Same as Fig. 13.

rors in choice of V_0 is reduced, since a larger number of spectral peaks must be simultaneously brought into coincidence, and this argues strongly in favor of using such averages.

VI. DISCUSSION

A. The use of r factors in LEED

The use of quantitative procedures for comparison of experiment and theory, as pioneered by Jona[8,10] and others[9,11-14], is an idea whose time was clearly overdue. We have shown in this paper that simple measures of the variance of the fit between experimental and calculated intensity spectra are quite adequate for determination of optimum parameter values and have a potential advantage over alternative definitions in that a least-squares analysis of errors can be made. We emphasize that the reliability of the reliability indices is clearly greater when an average over several (hk) beams is used.

An additional potential advantage of the use of r factors in LEED analyses, as stressed by Zanazzi and Jona,[10] is their usefulness in assessing the reliability of different structure determinations. In this respect, however, it seems evident to us that an absolute r factor scale to take into account all the factors that may differ from one structure determination to the next can only be defined in a rather arbitrary manner. The problem lies in the difficulty in quantifying the information content of a collection of LEED data. For example, hypothetical LEED intensities measured for the (111) planes of platinum and nickel for the same number of beams and energy ranges could be argued to have different information contents in the sense that the larger layer spacing in the case of platinum should result in a more dense distribution of peaks along the energy axis of the spectra, but it is not obvious that such a difference can be assigned a meaningful numer-

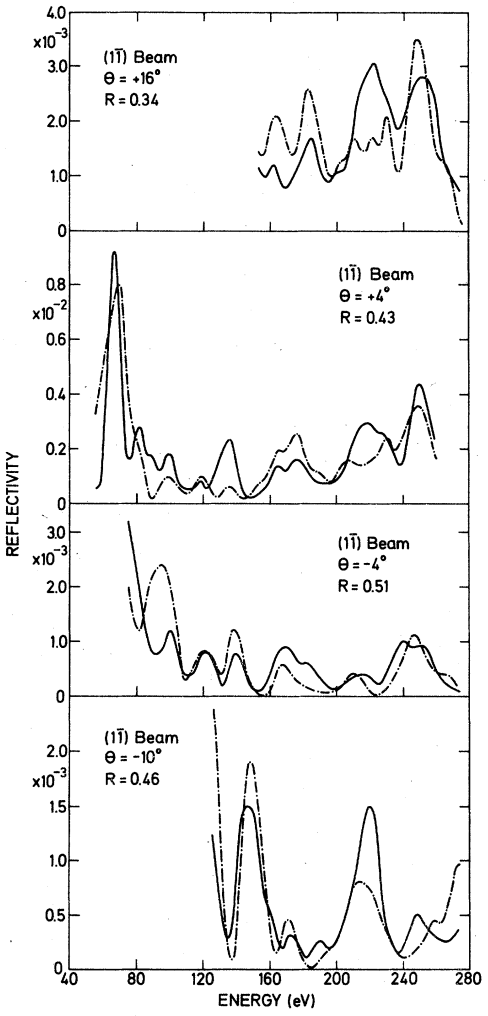

FIG. 18. Same as Fig. 13.

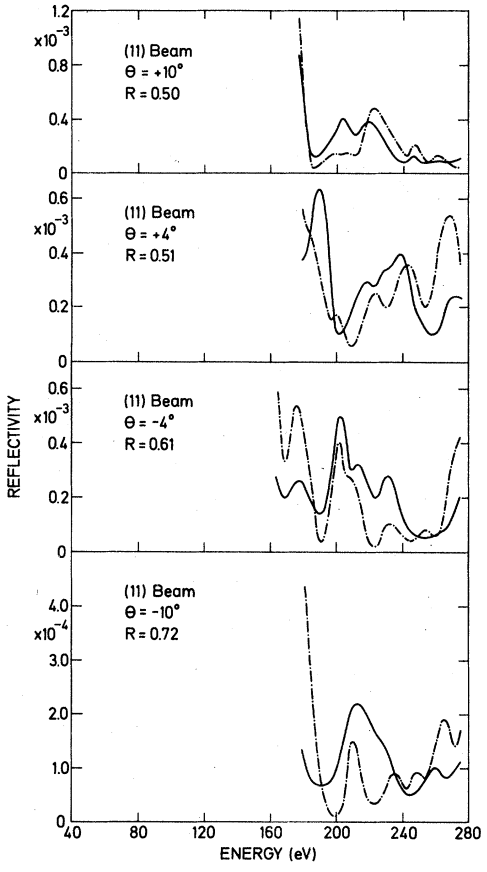

FIG. 19. Same as Fig. 13.

ical value.

In view of such difficulties, we doubt the usefulness of reduced r factors designed to account for different numbers of beams, energy ranges, etc. In the respect, we consider that the simple R_1 factors defined in Eqs. (5.2) and (5.9) are adequate to enable a rough judgment of the reliability of a structure determination to be made. In the case where the R_1 factors are calculated with scale factors w defined by Eq. (5.5), they they are bounded by zero and two for the cases of perfectly correlated and perfectly anticorrelated pairs of spectra. The average R_1 factor for the normal incidence spectra shown in the Appendix is 0.34, and the average over the entire set of spectra is 0.40. The corresponding numbers when a single scale factor $\overline{w}$ is used are 0.43 and 0.52 respectively. We have not (intentionally) investigated the range of values for randomly correlated spectra, but various mistaken comparisons and a plot of $\overline{R}_1$ vs $d_\perp$ similar to that shown for $\overline{R}_2$ in Fig. 3 suggest the range to be $\overline{R}_1 = 0.7$–1.0.

B. Accuracy of structure determination

We believe that the level of agreement between experimental and calculated intensity spectra achieved here for Pt(111) is close to the current state of the art of LEED analyses for high-z elements. It is a fact, nevertheless, that the $\overline{R}_1$ factor of 0.34 for the normal incidence spectra, for which the most accurate calculations were possible, compares unfavorably with $\overline{R}_1$ factors of 0.1 or less typically achieved in x-ray crystallography.

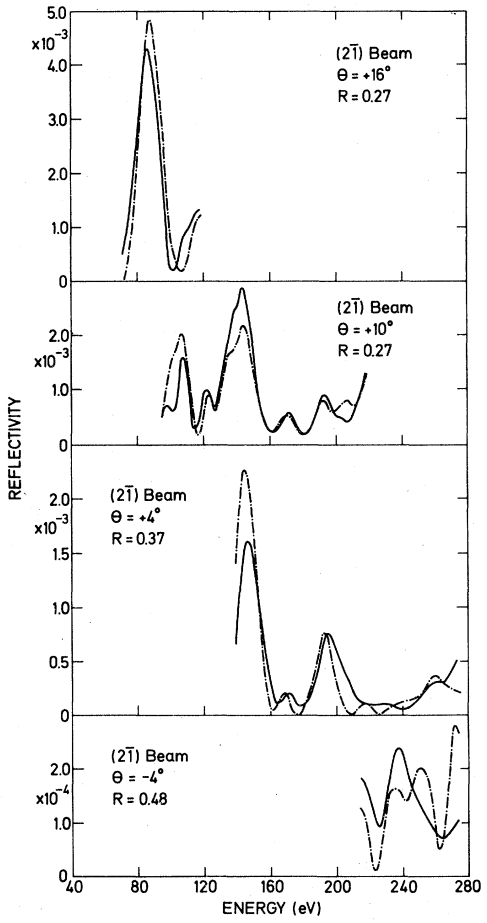

FIG. 20. Same as Fig. 13.

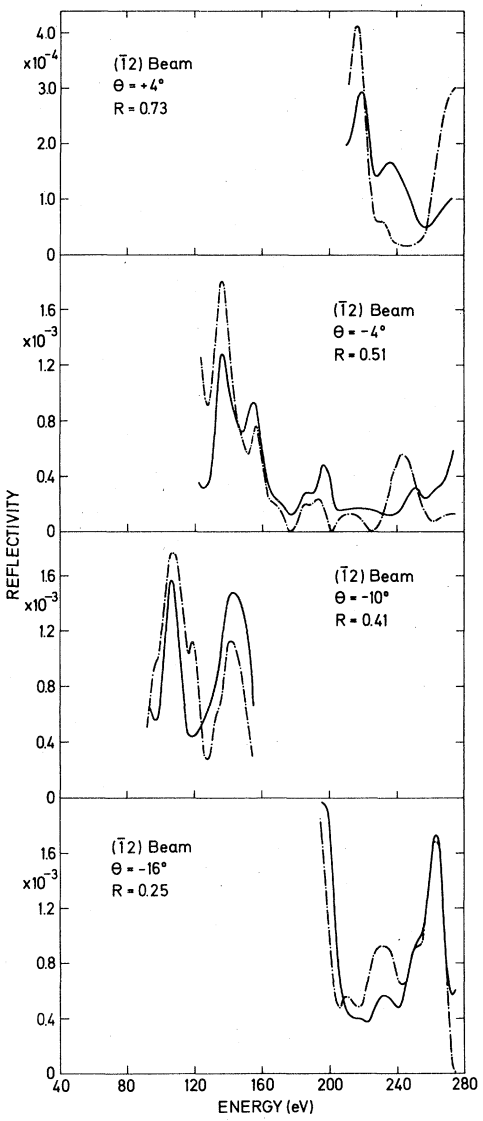

FIG. 21. Same as Fig. 13.

It seems unlikely in view of the determined variations in r factors with the model parameters that the level of agreement is limited by choice of optimum parameter values. The relative insensitivity of the agreement to the values of the nonstructural parameters V_0, V_{im}, and Θ_D suggests that inclusion of an energy dependence of V_0 and V_{im} and a layer dependence of Θ_D would not significantly improve the agreement, although such dependencies have not been investigated in the present work. The results of Fig. 4 suggest that failure to include enough phase shifts in representing ion-core scattering cannot be the limiting factor in the level of agreement. Similarly, the relatively small overall improvement produced by use of "quasirelativistic" phase shifts would seem to rule out relativistic effects as being the determining factor.

As far as the calculations are concerned, we are forced to presume that the ion-core potential itself is the dominant source of error. The most likely source of experimental error is probably the inability to prepare perfectly planar and defect-free surfaces. However, the magnitude of the errors resulting from these causes is impossible to determine, and in any event unlikely to be diminished in the near future.

Whatever the origin of the remaining discrepancy between experiment and theory, it would be desirable to have a clearer understanding of its consequences for the accuracy of structure determination via LEED than seems to be currently possible. In Sec. V, we presented an analysis of intensity spectra for five diffracted beams at normal incidence for Pt(111), which yielded a value of $d_\perp = 2.29 \pm 0.01$ Å. Having reached this conclusion, based on accepted methods of least-squares minimization, it must be recognized that the estimate of the error is probably too small. In particular, the results for the individual diffracted beams, as discussed in Sec. V F, suggest that systematic errors may be five or six times larger than the determined standard deviation of $d_\perp$.

In the analysis as described, the error is determined by the curvature of the χ^2 plot at the minimum. In view of the fact that such plots may contain additional local minima (see Fig. 3), the question of accuracy should perhaps include consideration of the ability to resolve the true minimum and be judged perhaps by the half-width of the

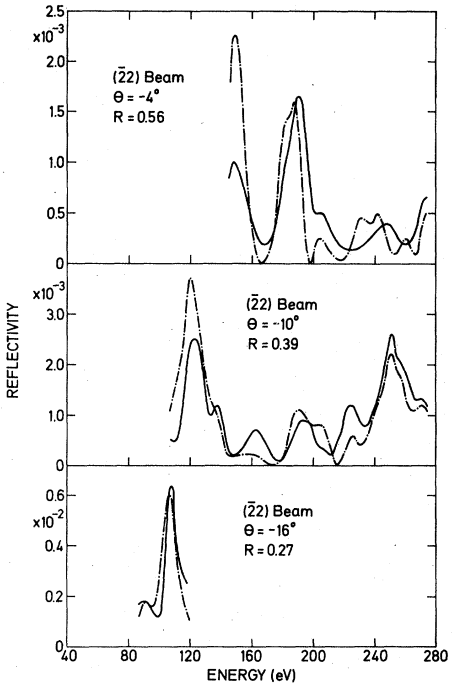

FIG. 22. Same as Fig. 13.

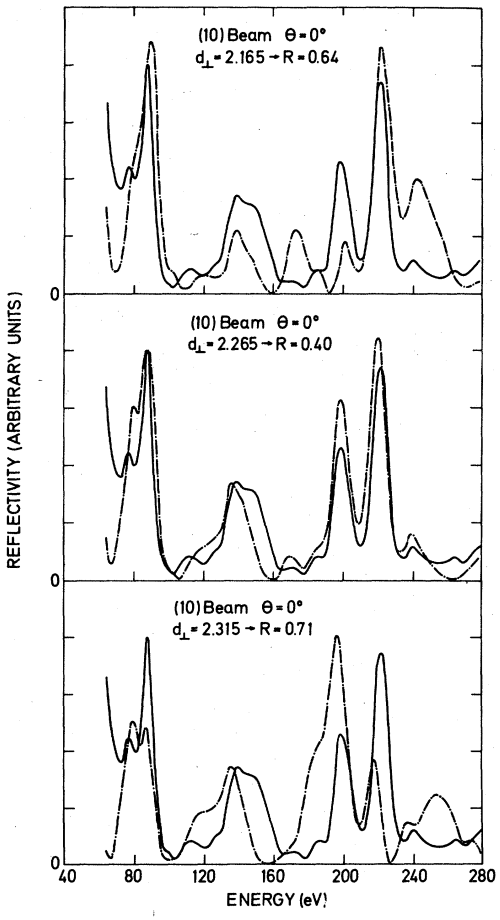

FIG. 23. Experimental intensity spectrum (solid line) for the (10) beam at normal incidence compared to calculated spectra for three values of $d_\perp$. The r factor is the R_1 factor.

global minimum. If this more conservative definition of the accuracy were adopted, the results of Fig. 2 would suggest an error in $d_\perp$ of about ±0.1 Å.

C. Nonstructural parameter values

Analysis of the fit between experimental and calculated intensity spectra for normal incidence, as described in Sec. V, leads to optimum values for the nonstructural variables of $V_0 = 5.4 \pm 0.6$ eV, $V_{im} = 5.2 \pm 0.4$ eV and $\Theta_D = 302 \pm 16°K$.

It is evident that the relative insensitivity of the fit to the values of the nonstructural variables (Fig. 9) leads to greater error in determination of optimum values than is the case for the structural variable $d_\perp$. The nominal errors quoted above are probably too small due to systematic errors associated partly with the lack of inclusion of the energy dependencies of V_0 and V_{im}, and the layer dependence of Θ_D.

ACKNOWLEDGMENTS

The authors wish to thank Professor Alex Ignatiev, University of Houston for invaluable assistance in developing and testing the experimental equipment used in this work. Dr. Roland Feder, Den Kernforschungsanlage, Jülich, kindly provided the relativistic Pt phase shifts used in some of the calculations. Mr. Bernard Addis, Cornell University, is thanked for providing the Pt(111) crystal used in the experiments. The Danish Natural Science Research Council is gratefully acknowledged for support of the experimental studies under Grant No. J. Nr 511-7080, and the computational work under Grant No. J.Nr. 511-10558. One of us (D.L.A.) wishes to acknowledge the hospitality of the Department of Physics, University of Houston, where the final version of this manuscript was prepared.

APPENDIX

A summary of the comparison between experimental and calculated intensity spectra for Pt(111) is given in Table IV. The calculated spectra were obtained using "near-optimum" parameter values of

$$d_\perp = 2.265 \text{ Å (bulk value)}, \quad V_0 = 7.0 \text{ eV},$$

$$V_{im} = 5.0 \text{ eV}, \quad \Theta_D = 260°K.$$

These values are to be compared with the "optimum" values determined as described in Sec. V to be

$$d_\perp = 2.29 \pm 0.01 \text{ Å}, \quad V_0 = 5.42 \pm 0.57 \text{ eV},$$

$$V_{im} = 5.18 \pm 0.42 \text{ eV}, \quad \Theta_D = 302 \pm 16°K.$$

The R_1 factors in Figs. 11–23 and Table IV were calculated via Eq. (5.2), using individual scale factors w given by Eq. (5.5).

Normal-incidence intensity spectra are shown in Figs. 11 and 12. Nonnormal incidence spectra are shown in Figs. 13–22. Finally, in Fig. 23 an experimental intensity spectrum for the (10) beam at normal incidence is compared to calculated spectra for three values of $d_\perp$, to illustrate the sensitivity of the agreement to this parameter.

In Figs. 11 to 23 the experimental spectra are shown as solid lines, and the calculated spectra as dashed lines. The r factor given on each figure is the R_1 factor.

[1] P. C. Stair, T. J. Kaminska, L. L. Kesmodel, and G. A. Somorjai, Phys. Rev. B 11, 616 (1975); L. L. Kesmodel and G. A. Somorjai, *ibid.* B 11, 630 (1975).
[2] L. L. Kesmodel, P. C. Stair, and G. A. Somorjai, Surf. Sci. 64, 342 (1977).
[3] J. A. Davies, D. P. Jackson, N. Matsunami, P. R. Norton, and J. U. Andersen, Surf. Sci. 78, 274 (1978).
[4] D. L. Adams, H. B. Nielsen, and M. A. Van Hove, (unpublished).
[5] J. B. Pendry, *Low-Energy Electron Diffraction* (Academic, New York, 1974).
[6] M. A. Van Hove and S. Y. Tong, *Surface Crystallography by Low-Energy Electron Diffraction* (Springer-Verlag, Berlin, 1979).
[7] D. W. Jepsen, P. M. Marcus, and F. Jona, Phys. Rev. B 5, 3933, (1972).
[8] A. Ignatiev, F. Jona, D. W. Jepsen, and P. M. Marcus, LEED 7 Seminar Notes, Am. Phys. Soc. Meeting, San Diego, March 19–21, 1973 (unpublished).
[9] M. A. Van Hove, S. Y. Tong, and M. H. Elconin, Surf. Sci. 64, 85 (1977).
[10] E. Zanazzi and F. Jona, Surf. Sci. 62, 61 (1977).
[11] D. L. Adams and U. Landman, Phys. Rev. B 15, 3775 (1977).
[12] P. R. Watson, F. R. Shepherd, D. C. Frost, and K. A. R. Mitchell, Surf. Sci. 72, 562 (1978).
[13] R. W. Streater, W. T. Moore, P. R. Watson, D. C. Frost, and K. A. R. Mitchell, Surf. Sci. 72, 744 (1978).
[14] F. R. Shepherd, P. R. Watson, D. C. Frost, and K. A. R. Mitchell, J. Phys. C 11, 4591 (1978).
[15] B. W. Holland and D. P. Woodruff, Surf. Sci. 36, 488 (1973).
[16] O. K. Andersen, Phys. Rev. B 2, 883 (1970).
[17] R. Feder, Surf. Sci. 68, 229 (1977).
[18] J. L. Beeby, J. Phys. C 1 82 (1968).
[19] S. Andersson and J. B. Pendry, Solid State Commun. 16, 563 (1975).
[20] P. R. Bevington, *Data Reduction and Error Analysis for the Physical Sciences* (McGraw-Hill, New York, 1969).